Experimental Mechanics
https://doi.org/10.1007/s11340-024-01118-1

SP ISS: MECHANICS OF AM

# Fatigue Damage Evolution in SS316L Produced by Powder Bed Fusion in Different Orientations with Reused Powder Feedstock

M. Kopec[1] · U. Gunputh[2] · G. Williams[2] · W. Macek[3] · Z.L. Kowalewski[1] · P. Wood[2]

Received: 20 February 2024 / Accepted: 17 September 2024


## Abstract

**Background** Metal Laser Powder Bed Fusion Melting (LPBF-M) is considered economically viable and environmentally sustainable because of the possibility of reusing the residual powder feedstock leftover in the build chamber after a part build is completed. There is however limited information on the fatigue damage development of LPBF-M samples made from reused feedstock.

**Objective** In this paper, the stainless steel 316 L (SS316L) powder feedstock was examined and characterised after 25 reuses, following which the fatigue damage development of material samples made from the reused powder was assessed.

**Methods** The suitability of the powder to LPBF-M technology was evaluated by microstructural observations and measurements of Hall flow, apparent and tapped density as well as Carr's Index and Hausner ratio. LPBF-M bar samples in three build orientations (Z – vertical, XY – horizontal, ZX – 45° from the build plate) were built for fatigue testing. They were then subjected to fatigue testing under load control using full tension and compression cyclic loading and stress asymmetry coefficient equal to -1 in the range of stress amplitude from ± 300 MPa to ± 500 MPa.

**Results** Samples made from reused powder (25 times) in the LPBF-M process exhibited similar fatigue performance to fresh unused powder although a lower ductility for vertical samples was observed during tensile testing. Printing in horizontal (XY) and diagonal (ZX) directions, with reused powder, improved the service life of the SS316L alloy in comparison to the vertical (Z).

**Conclusions** Over the 25 reuses of the powder feedstock there was no measurable difference in the flowability between the fresh (Hall Flow: 21.4 s/50 g) and reused powder (Hall Flow: 20.6 s/50 g). This confirms a uniform and stable powder feeding process during LPBF-M for both fresh and reused powder. The analysis of fatigue damage parameter, D, concluded cyclic plasticity and ratcheting to be the main mechanism of damage.

**Keywords** SS316L · Stainless steel · Fatigue · Additive manufacturing · Laser Powder Bed Fusion Melting (LPBF-M)

## Introduction

SS316L is widely used in many industrial sectors due to a combination of its relatively high mechanical properties, corrosion resistance, weldability, and formability with common applications such as body implants and heat exchangers [1]. SS316L is also known for its low thermal conductivity, high melting point, limited sensitivity to oxygen and high absorptivity in infrared, which make it an excellent material to produce by additive manufacturing, AM [2].

AM for SS316L involves different types of technologies including Powder Bed Fusion (PBF), Directed Energy Deposition (DED), Fused Deposition Modelling (FDM) and Binder Jetting (BJ) [3] among which PBF is the most commonly used AM process [4]. In PBF processes, it is common

✉ M. Kopec
mkopec@ippt.pan.pl

1 Institute of Fundamental Technological Research, Polish Academy of Sciences, Pawinskiego 5B, 02-106 Warsaw, Poland

2 Institute for Innovation in Sustainable Engineering, College of Science and Engineering, University of Derby, DE22 1GB Derby, UK

3 Faculty of Mechanical Engineering and Ship Technology, Gdańsk University of Technology, Narutowicza 11/12, Gdańsk 80-233, Poland

Published online: 26 September 2024

practice to reuse the unused powder in previous builds [5] which is both environmentally and economically beneficial [6]. However, the repeated reuse of powders can lead to their degradation reducing their quality, ultimately making the powder unsuitable for additive manufacturing. The degradation of powders is influenced by various factors such as the powder content, printing parameters and powder kinetics amongst others [5], making it difficult to determine a definitive end-of-life point for them. The most accurate way to assess powder quality is through the production and analysis of components using these powders. Delacroix et al. [7] and Heiden et al. [8] confirmed that SS316L powder could be successfully recycled 15 and 30 times respectively, to produce successive laser-based PBF prints. The effectiveness of the recycling process in terms of mechanical response was assessed through uniaxial tensile tests and microhardness measurements only [7]. Furthermore, Gorji et al. [9] proved that there are no significant changes in mechanical properties (microhardness) of AM SS316L parts and powder properties when powder is reused more than 10 times. The tensile properties examined in studies on powder reuse are mostly ultimate tensile strength, yield strength, and ductility in samples built vertically and horizontally. Anisotropic mechanical behaviour was observed due to the presence of equiaxed grains in horizontal samples and columnar grains in vertical samples [10, 11]. Nonetheless, there is limited knowledge on the fatigue behaviour of reused 316 L powder since most of the published works consider recycling suitability through static tensile test only [6]. Hence, there is a need to investigate the effect of reusing SS316L powder in a PBF process on the fatigue properties.

Uniaxial tensile tests performed on SS316L manufactured using Laser Powder Bed Fusion Melting (LPBF-M) [8], Directed Laser Deposition (DLD) [12], Laser Engineered Net Shaping (LENS) [13], High-Power Direct Laser Deposition [14] displayed superior properties for the horizontal and 45° orientation over the vertical orientation of the build direction. Similar observations were made for the fatigue behaviour of AM SS316L whereby samples in horizontal [15] and 45° orientations [16, 17] exhibited enhanced fatigue behaviour as compared to vertically built samples. It is noted that the effect of build orientation on SS316L fatigue behaviour was mainly examined based on the S-N curve approach where stress-controlled fatigue tests were adopted. Douglas et al. [18] investigated recycled SS316L powder and used hot isostatic pressing to improve fatigue properties. This approach provides only limited knowledge reflected by the number of cycles to failure as a function of the stress amplitude applied. There has been no investigation on the evolution of fatigue damage parameters for PBF SS316L in the different build orientations.

Therefore, this paper aimed to study the orientation effects on the fatigue behaviour and dynamics of fatigue damage development (FDD) of PBF SS316L made from reused powder. First, the virgin and reused powder were characterised using grain size distribution, flow rate, apparent density, tapped density, Carr's index and Hausner ratio. Subsequently, the reused powder was used to build fatigue test samples in 3 build orientations following which a quantitative approach was used to determine the fatigue damage measure ϕ and the fatigue damage parameter D for LPBF-M SS316L samples made from the reused feedstock. The evolution of these parameters was studied in subsequent cycles for each direction independently to reflect the dynamics of FDD. This would significantly expand the state of the art in AM of 316 L for its potential applications in industrial AM after several reuses.

## Materials and Methods

### Powder Feedstock

Virgin SS316L powder feedstock was supplied by Renishaw [19]. Once used in an LPBF-M process, the unused SS316L powder was first collected. They were then sieved in a Russell Finex sieve (model MS400) with a mesh size of 63 µm before being reused to remove the small, satellite powder particles and any oxides [6].For every LPBF-M process the default print parameters provided by the software, Renishaw Quant AM, associated with the input CAD file, were used. The chemical element composition of the powder feedstock was determined using Inductively coupled plasma-optical emission spectrometry (ICP-OES) in both the fresh unused condition and in the reused condition according to UKAS ATM150, and the results are displayed in Table 1. The reused powder (R) had seen 25 reuses over several years in the powder bed and the occasional blending with a very

**Table 1** The chemical composition of SS316L powder (wt%)

| SS-316 L | Al | As | Cr | Cu | Fe | Mo | Nb | Ni | *P* | Si | Sn | Ti | V |
|---|---|---|---|---|---|---|---|---|---|---|---|---|---|
| Fresh, F | <0.01 | <0.01 | 18.1 | 0.03 | 66.2 | 2.38 | <0.01 | 12.7 | <0.01 | 0.63 | <0.01 | <0.01 | 0.026 |
| Reused, R | <0.01 | <0.01 | 18.2 | 0.084 | 65.9 | 2.38 | <0.01 | 12.7 | <0.01 | 0.65 | <0.01 | <0.01 | 0.035 |
| Fe | Cr | | Ni | | Mg | N | | O | | C | | S | |
| bal | 16–18 | | 10–14 | | ≤2 | ≤0.10 | | ≤0.10 | | ≤0.03 | | ≤0.03 | |

small quantity of fresh powder (F), typically topped up with an F/R ratio < 2% to maintain the volume needed for the powder bed.

### Characterisation of SS316L Powder Feedstock

The fresh and sieved reused powder was viewed under the scanning electron microscope, TESCAN VEGA 3. A monolayer of the respective powder were spread on a flat clean surface, following which a stub with a carbon tape was pressed lightly on the individual powders to pick up the powder particles. Loosely bound particles were removed by a compressed gas. The stubs with the fresh and sieved reused powder were then viewed under the SEM following which the size of the particles was analysed. The SEM images are shown in Fig. 1(a-b). The fresh powder particle size distribution was found to be normal and the average diameter at 10% and 90% in the distribution was respectively 16.8 and 46.7 µm, which is close to the supplier's sieve size range from 15 to 45 µm at 10% and 90% for this powder [19]. Although some satellites sticking to the spherical powder particles could be found, their dimensions did not affect the average powder size. On the other hand, the reused powder feedstock presented in Fig. 1(c-d) was characterized by a developed surface containing agglomerates of melted particles among which, some non-deformed, unused particles could be found.

The reused powder was found to display particle average diameter of 18.0 µm and 48.3 µm at 10% and 90% of the distribution, which is only marginally larger than the fresh powder. This was similar to those obtained by Delacroix et al. [7] which was an average diameter of 23.2 µm and 47.3 µm at 10% and 90% of the distribution. The significant changes in the particles' shapes are related to the spattering of unmelted powders when exposed to the laser heat source during the LPBF-M process in the previous builds, which then attached to unaffected powders [20].

The flow rate was measured using a Qualtech QPI-HFM 1800 Hall Flowmeter according to ASTM B213-13. Apparent density, tapped density, Carr's index and Hausner ratio were determined using a Copley Scientific JV200i Tapped Density Tester according to the ASTM B527-23. The results are shown in Table 2. Comparable results were obtained for both types of powder. The most important features concerning satisfactory powder flowability were confirmed through Carr's index and Hausner's ratio, for which excellent and good free-flow values should range from 0 to 15 and 1.00–1.18, respectively. Hence, it could be concluded that the reused powder meets the technical requirements to be reused.

The chemical composition measurements of carbon, sulphur, oxygen, nitrogen and hydrogen contents by three independent laboratories are presented in Table 3. It confirmed

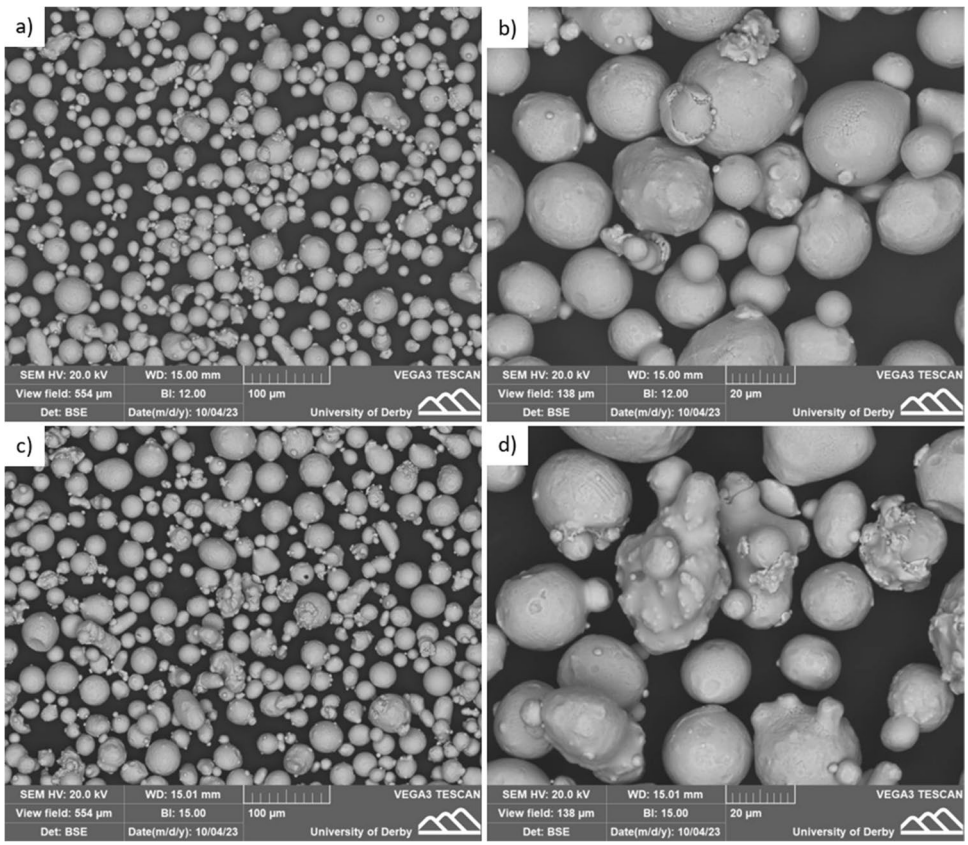


**Fig. 1** The SEM images (at low and high magnification) of fresh (**a**, **b**) and reused (**c**, **d**) powder feedstock

**Table 2** The comparison of fresh and reused SS316L powder characteristics

| | Hall flow (secs/50 g) | | Apparent density (g/cm$^3$) | | Tapped density (g/cm$^3$) | | Carr's index | | Hausner ratio | |
|---|---|---|---|---|---|---|---|---|---|---|
| | Mean | RSD ±% | Mean | RSD ±% | Mean | RSD ±% | Mean | RSD ±% | Mean | RSD ±% |
| Fresh | 21.4 | 2.58 | 4.762 | 0.00 | 5.085 | 1.45 | 6.35 | 1.37 | 1.068 | 0.02 |
| Reused | 20.6 | 2.39 | 4.762 | 0.00 | 5.310 | 1.54 | 10.31 | 1.37 | 1.115 | 0.02 |

**Table 3** The chemical composition analysis of particular elements for fresh and reused powder

| | Carbon | | | Sulphur | | | Oxygen | | Nitrogen | | Hydrogen | |
|---|---|---|---|---|---|---|---|---|---|---|---|---|
| | (%) Weight | | | | | | | | | | | |
| Required Specification [19] | ≤0.03 | | | ≤0.03 | | | ≤0.10 | | ≤0.10 | | - | |
| Fresh | 0.022 | 0.025 | 0.022 | 0.010 | 0.004 | 0.006 | 0.033 | 0.045 | 0.105 | 0.097 | <0.0005 | 0.00014 |
| Reused | 0.023 | 0.022 | 0.022 | 0.009 | 0.005 | 0.005 | 0.042 | 0.040 | 0.098 | 0.095 | <0.0005 | 0.00021 |
| | (RL) | (SAS) | (B) | (RL) | (SAS) | (B) | (SAS) | (B) | (SAS) | (B) | (SAS) | (B) |

the acceptable content of all investigating elements in terms of their percentage and parts per million contents. The results elaborated for fresh and reused powders were below the limits specified by the material supplier, and therefore, its application in the LPBF-M process was confirmed.

It is not environmentally and economically viable to waste used metal powders in AM processes. Although it is difficult to predict the degradation of reused powder for AM [21], the morphology and properties of the reused powder were well within the recommended range by the material supplier and very close to the virgin powder in this study. Hence, the SS316L reused powder was considered viable to be used for the LPBF-M process. Nonetheless, the effect of reusing the powder, 25 times, needs to be assessed on fatigue behaviour.

## Additive Manufacturing of SS316L Test Samples

Rectangular samples (25 by 130 mm) and cylindrical specimens of diameter and length equal to 10 mm and 56 mm, respectively, were additively manufactured through a Laser Powder Bed Fusion Melting (LPBF-M) using the Renishaw AM 250 system (200 W power, 70 µm spot size, and 1070 nm wavelength). The reused powder was used for these builds.

The rectangular samples were built in vertical (Z), and horizontal (XY) directions and the cylindrical bars were printed in three directions oriented with respect to the build plate (Z – vertical, XY – horizontal, ZX – 45°) (Fig. 2(a)) using the process parameters in Table 4. After the LBPF process, the as-built specimens were subjected to stress relief using a 470 °C soak for 6 h, whilst still attached to the build plate in accord with norms. The samples were then wire-cut from the build plate using a wire cut Electrical Discharge Machining process (AgieCharmilles Cut E 350), with a wire diameter of 0.1 mm to 0.3 mm and an axis speed ranging from 0 to 3000 mm/min. Subsequently, they were machined, using a lathe machine model Haas Automation ST-20Y to achieve the specimen geometry in Fig. 2(b) and c with respect to ASTM E8/8 M for the rectangular samples and ASTM Standard E606 for the cylindrical samples. For the gauge section in both tensile and fatigue samples, more than 2 mm thickness was removed shown in Fig. 1(b) and (c) respectively. This means the effect of the different microstructures from the border scan zone that used a higher laser energy density on the surface and subsurface was removed so that the residual microstructure can be associated exclusively with the volume fill hatch scanning parameters.

### Characterisation of AM SS316L Samples

Samples of 2 mm length were cut from the AM SS316 L rectangular pieces in the XY and Z direction and mounted in conductive resin. The mounted samples were polished using a 1 µm diamond surface finish and a Bakelite diamond grinding wheel flat of 1200 grit. Subsequently, they were etched in an electrolytic oxalic acid for a duration of 5 to 15 s. An Olympus BH2 optical microscope was then used to capture micrographs with the aid of a Lanopik Camera and Iworks Software.

## Quasi-Static Tensile Testing

The samples shown by yellow arrows (XY and Z) in Fig. 1(a) were machined to form tensile test samples as shown in Fig. 2(b) with respect to ASTM Standard E8/8 M. The uniaxial tensile test was carried out to determine the basic properties of the material including the conventional

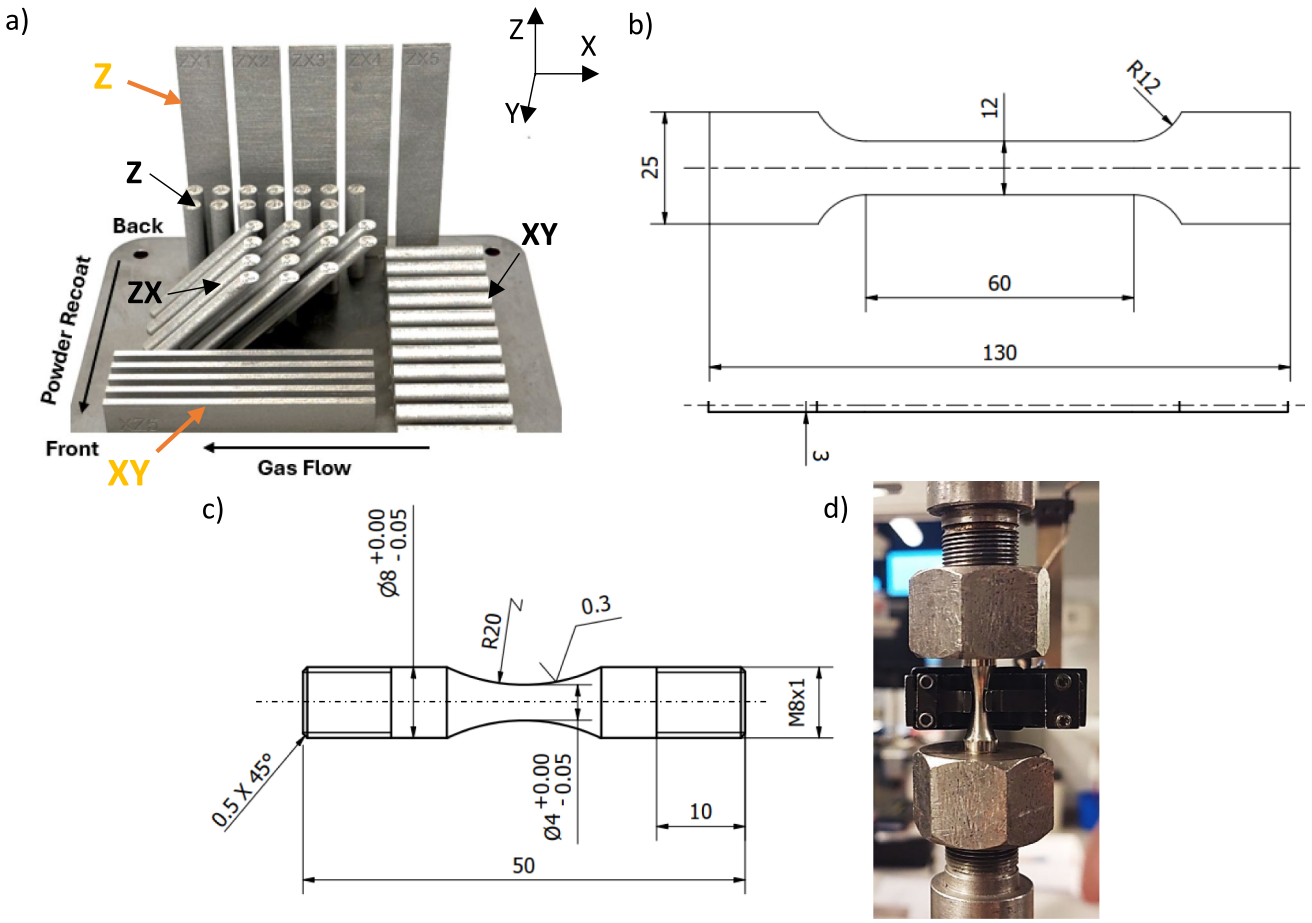


**Fig. 2** Printing orientation of specimens on the build plate (**a**); engineering drawing of the tensile test (**b**) and hourglass specimen for fatigue testing (**c**); the general view of the specimen fixed on the testing machine (**d**). (dimensions in millimetres)

**Table 4** Process parameters applied during AM

| Region | Layer thickness [μm] | Hatch distance [mm] | Beam comp [mm] | Focal point [mm] | Power [W] | Point distance [μm] | Exposure time [μs] | Scan speed [mm/s] | Energy density [J/mm$^3$] |
|---|---|---|---|---|---|---|---|---|---|
| Volume Fill Hatch | 50 | 0.11 | 0.025 | 0 | 195 | 60 | 80 | 750 | 47.27 |
| Scanning strategy | Meander | | | | | | | | |

yield strength (YS) $R_{0.2}$.using an MTS 858 machine with a load cell of 250 kN. Based on the YS value, the range of stress amplitude was established. Three uniaxial tensile tests per orientation were used to ensure the test reliability.

## Fatigue Testing

The general view of the specimen fixed in the testing machine grip was presented in Fig. 2(c).The MTS 858 uniaxial testing machine operated under force-control, zero mean level and constant stress amplitude of frequency equal to 20 Hz was applied to get the range of fatigue stress amplitude from ± 300 MPa to ± 500 MPa during fatigue testing. The fatigue test was allowed to run until failure. A transversal MTS extensometer was used to monitor changes in specimen diameter during the test. The axial strain was calculated by using Poisson's ratio equal to 0.33. To ensure the test reliability, three specimens per stress amplitude were used. Fatigue data was first represented by an S-N diagram relating the maximum stress to the number of cycles.

### Fractography

The fractured surfaces after both tensile testing and fatigue testing were viewed under a JOL6360 LA SEM equipped with the EDAX energy dispersive x-ray spectroscopy (EDS) detector for the chemical composition analysis. The topographic and backscatter electron modes were applied during observations. The whole cross-section of the fractured surface was first viewed followed by an in-depth high magnification imaging, which allowed the microstructures to be more visible. All samples were viewed, and one representative was presented in this paper.

## Experimental Results and Discussion

### LPBF-M SS316 L Characterisation

The optical micrographs of the vertical, Z, AM specimens consisted of the characteristic layers of melting pools as shown in Fig. 3(a). The presence of melt pools well overlapped with adjacent ones confirms that the laser density used during the LPBF-M process was sufficient. The diagonal overlapping path seen in the optical micrograph of the XY surface (Fig. 3(b)) resulted from the 67° rotation of the laser path from which the subsequent layers were scanned. This is representative of the meander scanning strategy used in this study.

### Quasi-Static Tensile Testing

The uniaxial tensile test results are presented in Fig. 4(a). With exception to the elongation of Z, these results were found similar to those reported in [22] for the same LPBF-M process and different printing strategies, as well as for LENS-manufactured ones [13]. Other works [19, 23] reported the elongation of LPBF-M 316 L in Z exceeds 20% depending on the heat treatment, although the variability is higher in Z than in XY. The difference in the strength was attributed to the print orientation as the loading direction in XY samples was parallel to the sliced layers in which

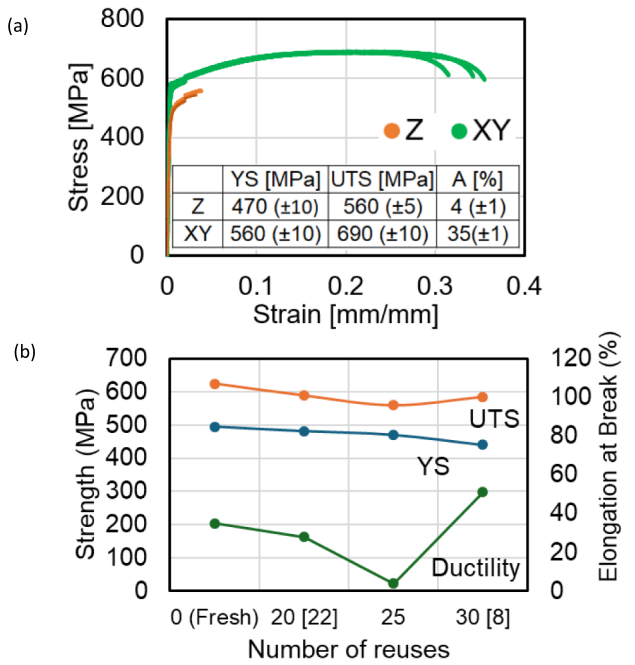


**Fig. 4** Tensile characteristics of the additively manufactured SS316L printed in different directions (**a**) and the tensile properties of vertically built LPBF SS316L samples with respect to the number of reuses [8, 23] where 25 reuses data is from this work (**b**)

the scanning tracks served as fibres that reinforced the bulk material [14]. On the other hand, for the vertical direction, the loading orientation is normal to the sliced layers. Thus, the weak metallurgical bond between layers is responsible for the relatively lower values of tensile properties. Simultaneously, in the Z direction, the load is perpendicular to any potential micro/macro-cracks formed between the layers. Consequently, cracks may propagate suddenly even at relatively low elongations.

The elongation at break for the Z samples (4%) is significantly lower than reported in the literature [22], with previous work [23] and supplier data [19] reporting more than 25%. The printing parameters used in this work are similar to those used in the work by Kunz et al. (2017) [24] which was considered to be the optimum parameter to minimise density.

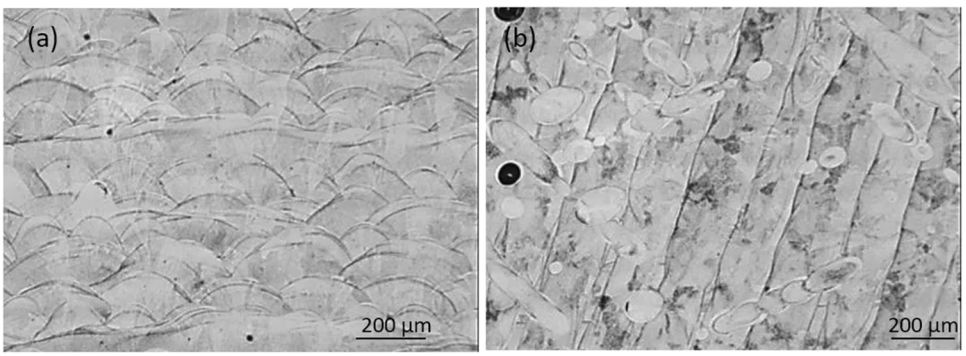


**Fig. 3** Optical micrographs of the as-built alloy observed along the parallel (Z) (**a**) and perpendicular (XY) (**b**) to the building orientation

Moreover, the taller Z tensile test samples were built at the back of the build plate, as shown in Fig. 2(a) for optimum tensile strength and elongation as identified by Kunz et al. [24]. The recoater motion spreads the powder from the back to the front of the build plate during the PBFL-M process. It is known that samples built at the end of the powder recoat (front of the plate) are known to have lower density and inferior mechanical properties [24, 25]. Contrarily in this work, the samples built at the back had lower elongation at break. This was associated with the reduced scan length of the taller Z samples after the majority shorter samples had been additively manufactured. As shown in Fig. 2(a), 61.5% of the height of the Z samples (including the gauge section) are manufactured with a 3 mm scan length for the cross-section. Such a short scan length has been shown to cause shrinkage across the width of the samples [26], which accounted for the reduced ductility.

In all the works presented in Fig. 4(b), optimum printing parameters were chosen with respect to density and/or mechanical properties. While the samples from 30 reuses exhibited similar mechanical properties for Z and XY to this work, the elongation at break was higher for the Z samples [8]. Firstly, the lower scan length accounted for the low elongation at break in the current work. Secondly, Heiden et al. [8] proved that even after 25 uses, if the right printing parameters are selected, the mechanical properties of the AM samples can be maintained/enhanced. In that work, a low power of 100 W and a high scanning speed of 1400 mm/s was used. This combination [8] has been shown to result in samples with minimal porosity and higher density [27], which can account for such a high elongation at break.

## Fatigue Testing

Figure 5 shows the fatigue performance of the XY, ZX and Z samples. XY samples exhibited the best fatigue performance since, for both extreme stress amplitudes of ± 300 MPa and ± 500 MPa, the number of cycles to failure was from five to ten times higher, as compared to the two remaining directions considered (Fig. 5(b)). This beneficial improvement in the fatigue behaviour of the specimens printed in the horizontal direction was also reported for SS316L manufactured using DMLS [15], SLM [15, 16, 23, 28–30], LDW [12, 15] and LPBF-M [28, 31]. There are several potential reasons reported in the literature on the effect of build orientation on the fatigue life of machined specimens [1]:

- - since AM processes involve layer-by-layer printing strategies, more irregularities could be found on the vertical specimens' surfaces. These act as geometrical notches of sharp radii, and because of their perpendicular orientation to the loading direction, they are most likely the potential areas of crack initiation.
- - in SLM-manufactured steels, processing defects including porosities, are generally elongated perpendicularly to the printing direction, and consequently, specimens manufactured in horizontal orientation exhibit a higher share of small porosities. Such porosity distribution is also leading to the occurrence of interfacial weak links between layers and following the formation of planar defects.

The analysis of the fatigue behaviour of AM SS316L also involved the examination of hysteresis loop evolution in subsequent cycles to failure. Figure 5(c-h) illustrates three representative hysteresis loops: green from the beginning of the fatigue test, orange corresponding to the specimen's midlife and red registered before failure. The numbers displayed in Fig. 5(c-h) corresponds to a specific loading cycle. Based on the character of these loops, the main deformation mechanisms were determined for boundary stress amplitude values:

- For ± 300 MPa, ratcheting represented by the almost constant width of the initial hysteresis loop during testing and its shift in subsequent cycles (Fig. 5(c-e)).
- For ± 500 MPa, cyclic plasticity represented by significant changes in hysteresis loop width already observed in the initial cycles (Fig. 5(f-h)) without hysteresis loop shift.

The specimens examined in this study exhibited improved fatigue response compared to those LPBF-M manufactured in the vertical and horizontal orientations reported in [1, 2], which could be potentially attributed to the machining process post-LPBF. When similar printing parameters were used by Wood et al. [23], lower fatigue responses were observed. However, when the samples were machined the fatigue behaviour was enhanced in the latter study. This was associated with low roughness which improved the high cycle fatigue life of SS316L since the subsurface porosities and other defects formed during AM could be removed [12, 14, 17]. Since the surface roughness measurements were not performed in this research, its effect on fatigue response was not discussed in detail. However, the surface finish process was performed using a CNC lathe to ensure the high quality of the specimens and their geometrical accuracy. Although a stress relief heat treatment was applied to all specimens, any internal residual stress remaining in the AM material could be partially released by machining the outer part of the specimen. Consequently, the machined and polished specimens are characterized by a higher fatigue strength in comparison to the polished-only ones [32]. However, the surface quality is not the only parameter that affects the fatigue life of AM specimens. Other manufacturing

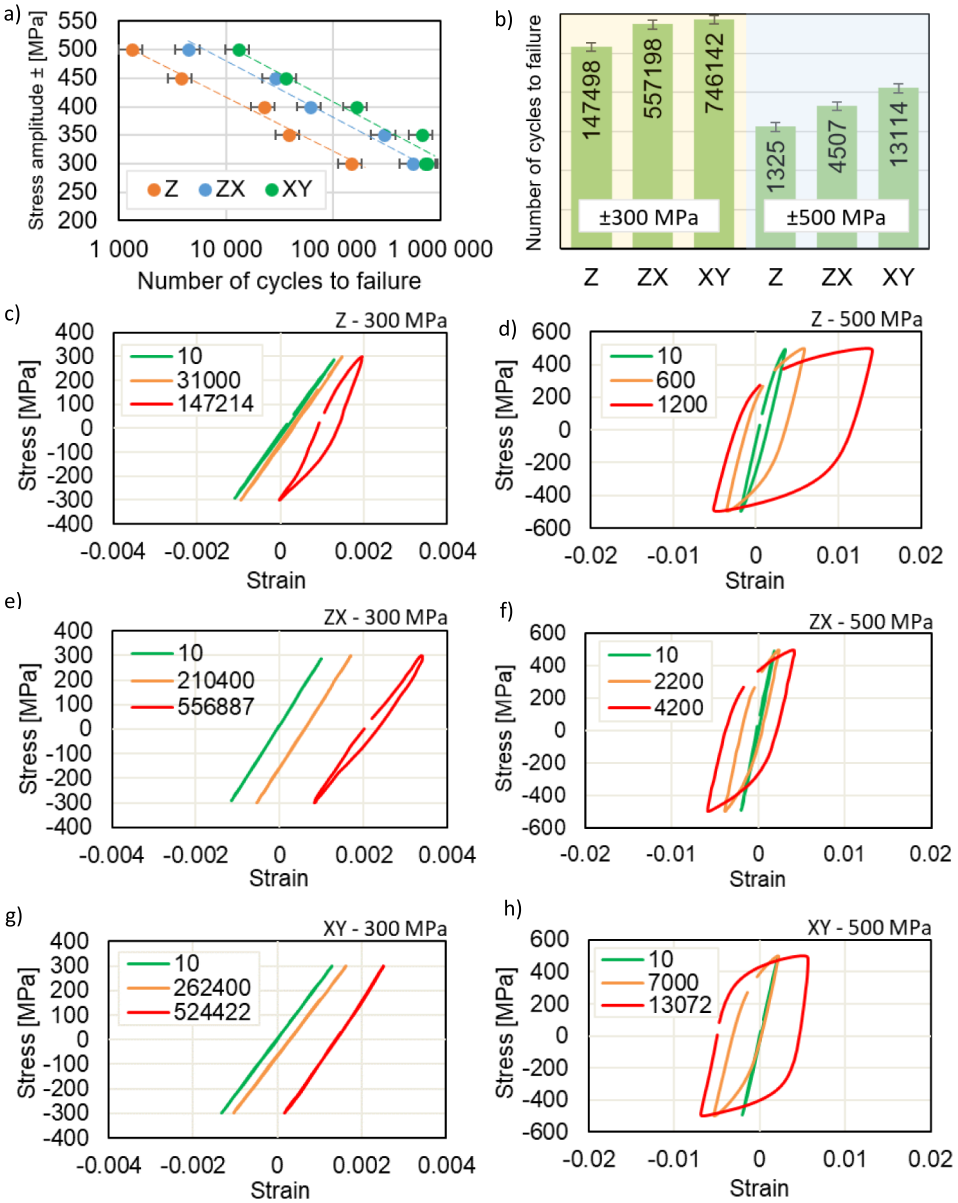


**Fig. 5** S-N characteristics of the additively manufactured SS316L printed in different directions expressed by stress amplitude and logarithmic representation of the number of cycles to failure (**a**); service life dependence on stress amplitude applied and printing strategy (**b**); fatigue response of AM SS316L printed in Z tested at the stress amplitude equal to ± 300 MPa (**c**) and ± 500 MPa (**d**); fatigue response of AM SS316L printed in ZX tested at the stress amplitude equal to ± 300 MPa (**e**) and ± 500 MPa (**f**); fatigue response of AM SS316L printed in XY tested at the stress amplitude equal to ± 300 MPa (**g**) and ± 500 MPa (**h**). (The numbers displayed correspond to a specific loading cycle)

process parameters including the building orientation and heat treatment applied also affect the fatigue life [1].

In this research, a difference in the number of cycles to failure was around 25% for the same stress amplitude applied in each printing orientation considered (Fig. 5(a)). Therefore, it was concluded that the proposed process parameters could be successfully used to manufacture the specimens of similar service life. The significant scatter of fatigue life for SS 316 L found in the literature draws particular attention to the differences related to the several process-dependent factors and their subsequent effect on the service life of AM SS316L. Although many difficulties related to the repeatability of AM processes and fatigue tests themselves, the experimental results obtained in this work show that CNC high-precision machining enhanced the fatigue life of AM SS 316 L.

The increasing number of papers on fatigue life prediction of SS316L [33–35] highlights the importance of studies devoted to service life determination and expanding the knowledge on fatigue damage mechanisms under cyclic loading conditions. In this paper, the qualitative approach of fatigue damage development was proposed, and subsequently, assessed through the analysis of the SS316L mechanical response registered in the successive cycles under constant stress amplitude. The selected hysteresis loops were presented for the LPBF-M SS316L in three directions (Z, ZX and XY) tested at the extreme stress amplitudes equal to ± 300 MPa and ± 500 MPa to investigate

an influence of stress amplitude and state of material on the damage mechanism of the material tested (Fig. 5(c-h)). The three specific loops were selected for each condition: the initial loop captured at the beginning of fatigue, the loop registered for the steady state of FDD, when a slight strain increase over time was observed, and the loop preceding the specimen failure. The further analysis of hysteresis loop changes during fatigue testing exposed ratcheting and cyclic plasticity as the main mechanisms responsible for FDD [36].

These mechanisms could be distinguished based on the character of hysteresis loops registered in the subsequent cycles. When ratcheting is dominant during cyclic deformation, only slight changes in the hysteresis loop width are observed. However, a simultaneous increase in the mean level of strain can be found in the subsequent cycles. On the other hand, cyclic plasticity is characterized by considerable changes in the hysteresis loop width found in the subsequent cycles [37]. The main deformation mechanism observed at the stress amplitude of ± 300 MPa was ratcheting, since the width of the initial hysteresis loop remained almost constant during testing and its shift in subsequent cycles was observed only, (Fig. 5(c-e)). Interestingly, when the higher stress amplitude of ± 500 MPa was applied, the cyclic plasticity mechanism was found to be the dominant. The hysteresis loop width changes already observed in the initial cycles (Fig. 5(f-h)) were more evident in the following cycles.

The strain evolution in the subsequent cycles was also used to expose the FDD dynamics (Fig. 6(a-b)). It was

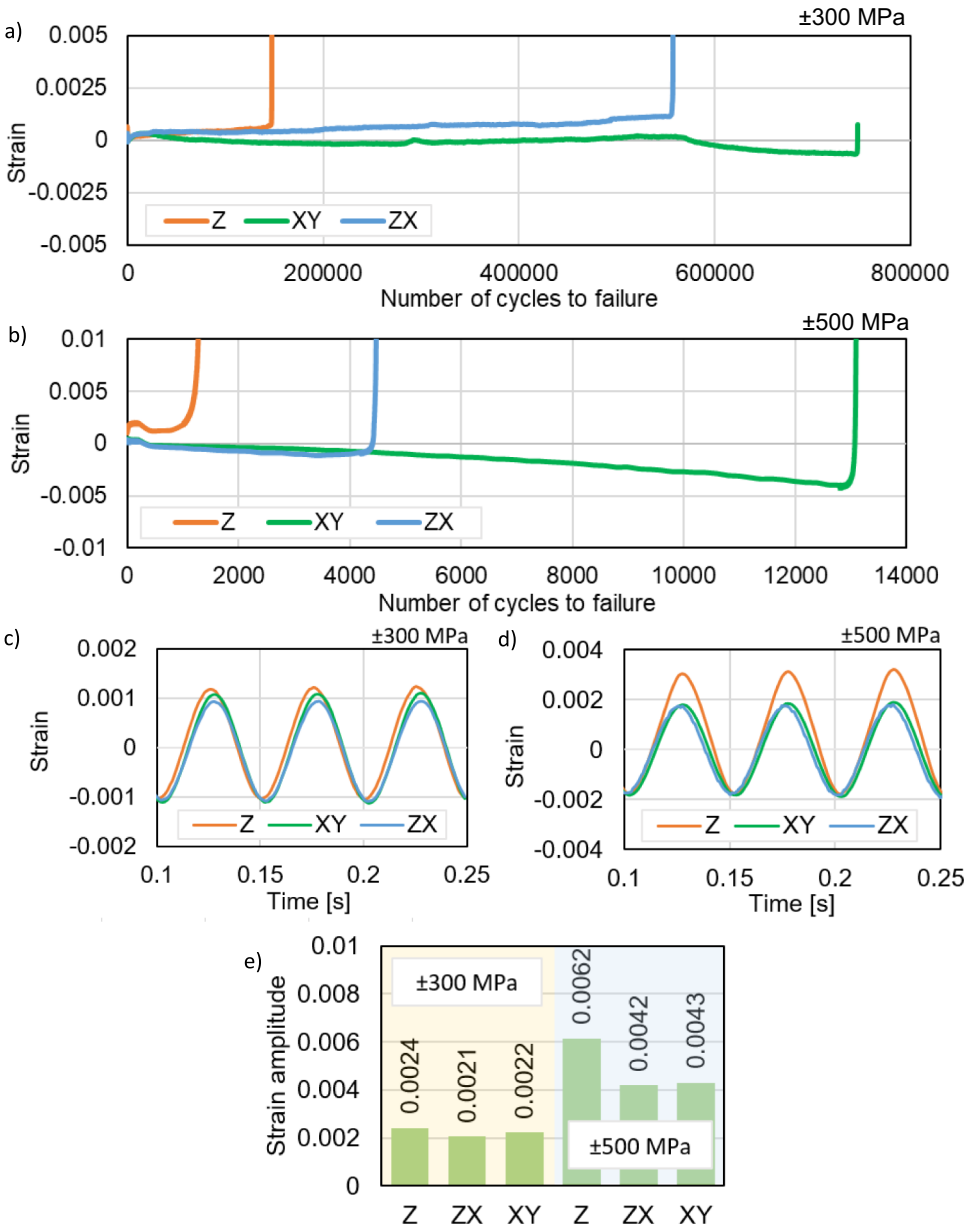


**Fig. 6** Strain-number of cycles to failure relation for the SS316L specimens tested at the stress amplitude equal to ± 300 MPa (**a**) and ± 500 MPa (**b**). The strain-time response of the SS316L specimens tested at the stress amplitude equal to ± 300 MPa (**c**) and ± 500 MPa (**d**); strain amplitude values registered for the same time range (**e**)

observed that regardless of the stress amplitude used, the specimen manufactured in the Z direction exhibited an increase in strain much earlier than the specimens built in the ZX and XY directions. The behaviour of ZX and XY display stable strain increases up to specimen fracture. A decrease in strain values registered for the XY specimen after $6 \times 10^5$ cycles was probably related to a slip of the extensometer legs during fatigue testing.

The fatigue testing at the stress amplitude of $\pm 300$ MPa was analysed in terms of the strain-time response, however, these changes were not that pronounced as compared to testing at $\pm 500$ MPa (Fig. 6(c-e)). The AM specimens printed in XY and Z directions were again characterized by the lowest strain response about the stress amplitude applied.

## Fractographic Observations

The fractographic observations performed on 316 L tensile specimens manufactured in XY (Fig. 7(a-b)) and Z (Fig. 7(c-d)) orientations after the tensile test exhibited significantly different fracture mechanisms. Plastic deformation was observed for horizontally manufactured specimens (Fig. 7(b)) with the presence of equiaxed dimples on the surface. For the vertical, Z samples (Fig. 7(c)(d)), intergranular mode was observed and unmelted particles (circles) and bigger pores (arrows) were visible which altogether accounts for the lower ductility presented in Fig. 4. Unmelted particles and intergranular fracture mode was probably caused by the rapid solidification during AM. Furthermore, observations performed on the side of the Z-manufactured specimen (Fig. 7(e)) revealed elongated cracks formed perpendicularly

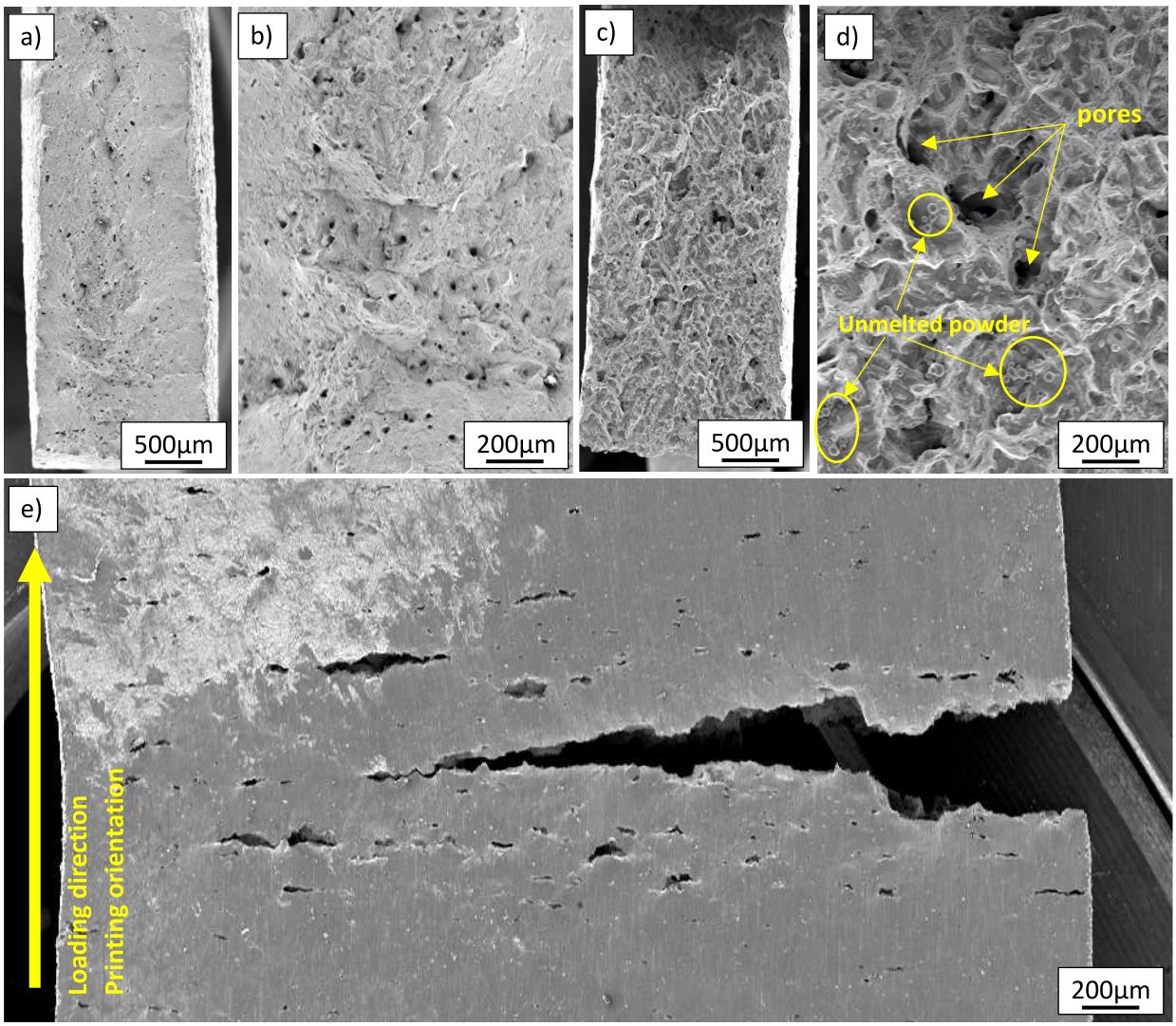


**Fig. 7** Fracture surfaces of 316 L specimens manufactured in XY (**a**, **b**) and Z (**c**, **d**) orientations after tensile test; side view of the Z orientation with notable cracks in the direction perpendicular to the loading (**e**)

to the loading direction along the printing strategy applied. It was related to the fact that the manufacturing of relatively flat specimens in the vertical direction may expose the printing paths since the heat exchange during the process is not sufficient. Further analysis needs to be done for vertical LPBF-M SS316L samples built at different locations on the build plate with the respective density analysis.

Fracture surface observations of AM specimens subjected to fatigue provide detailed information about damage mechanisms responsible for specimen failure [32, 38]. Analysis of the topographic view of the SS316L specimens exposed the classical fracture areas for all printing directions: initiation area characterized by the radial streaks found along the crack propagation direction followed by smooth facet flaws; propagation area with a notable number of micro voids and dimples; instantaneous area of the highest material instability leading to its fracture. The crack was initiated at the edge of the specimen, where the sub-surface defects or non-metallic inclusions were observed (Figs. 8 and 9). These inclusions act as stress concentrators, and therefore, crack initiation occurs favourably in such areas.

The propagation area consisted of characteristic features including microvoids and secondary cracks that occurred due to joining pores. Ductile fracture surfaces of the trans-crystalline fracture mode and fine morphological cavities were observed more in the AM specimens subjected to the lower stress amplitude of ± 300 MPa as compared to those subjected to ± 500 MPa (Fig. 9). Conversely, cleavage steps created in parallel to the crack propagation direction formed river patterns, which can be indicated in all AM specimens, regardless the value of stress amplitude applied and build orientation.

The crack nucleation region in the Z samples (± 300 MPa) was observed just below its surface, where the inclusion was found (Fig. 9(a)). In the surrounded areas, unmelted particles, cleavage facets and tear ridges are clearly visible. Different fracture mechanisms were observed in samples built in different orientations. For the ZX specimens fractured in the

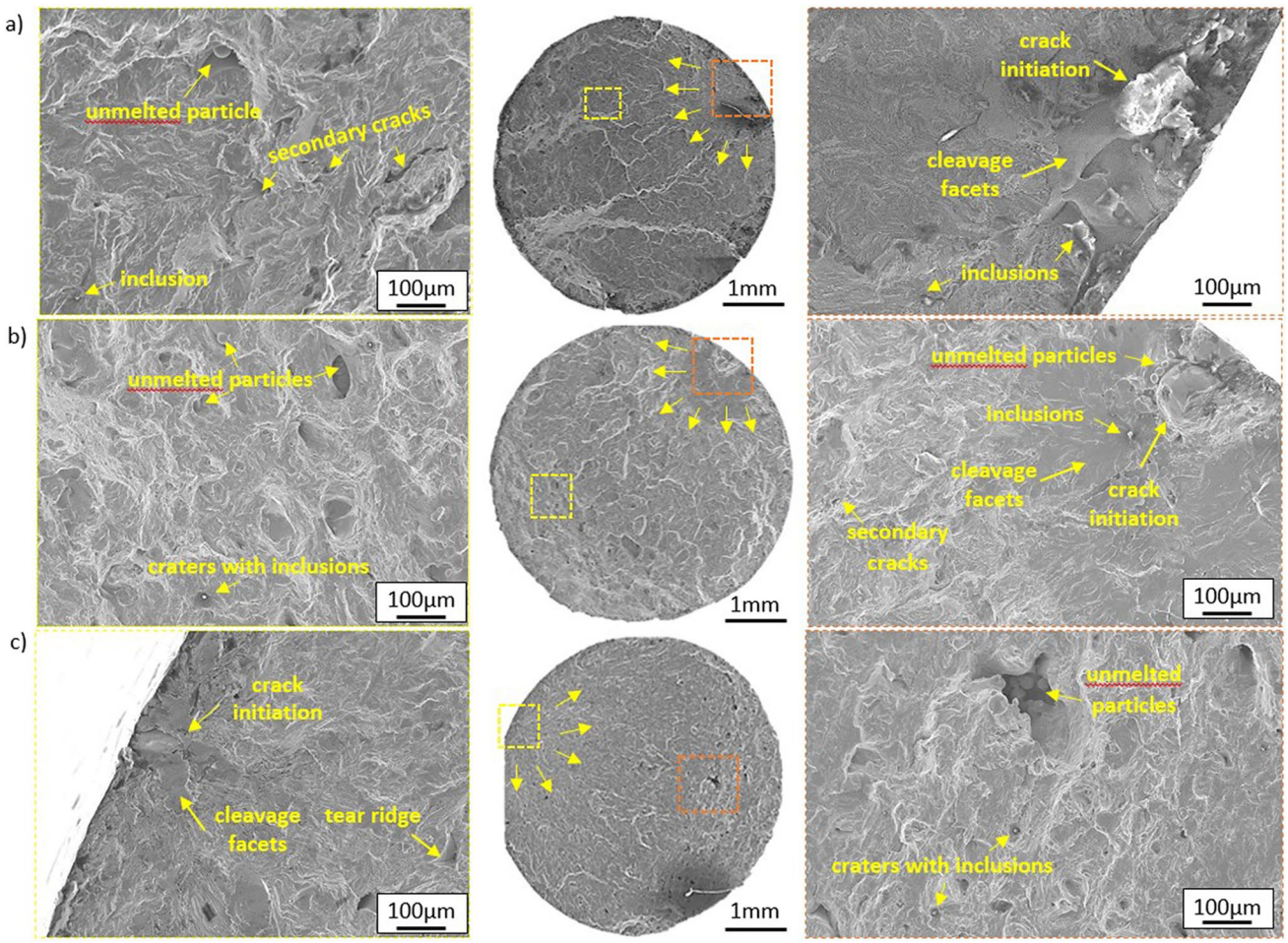


**Fig. 8** Fracture surfaces of SS316L specimens manufactured at Z (**a**), ZX (**b**), and XY (**c**) directions and tested at the stress amplitude equal to ± 500 MPa

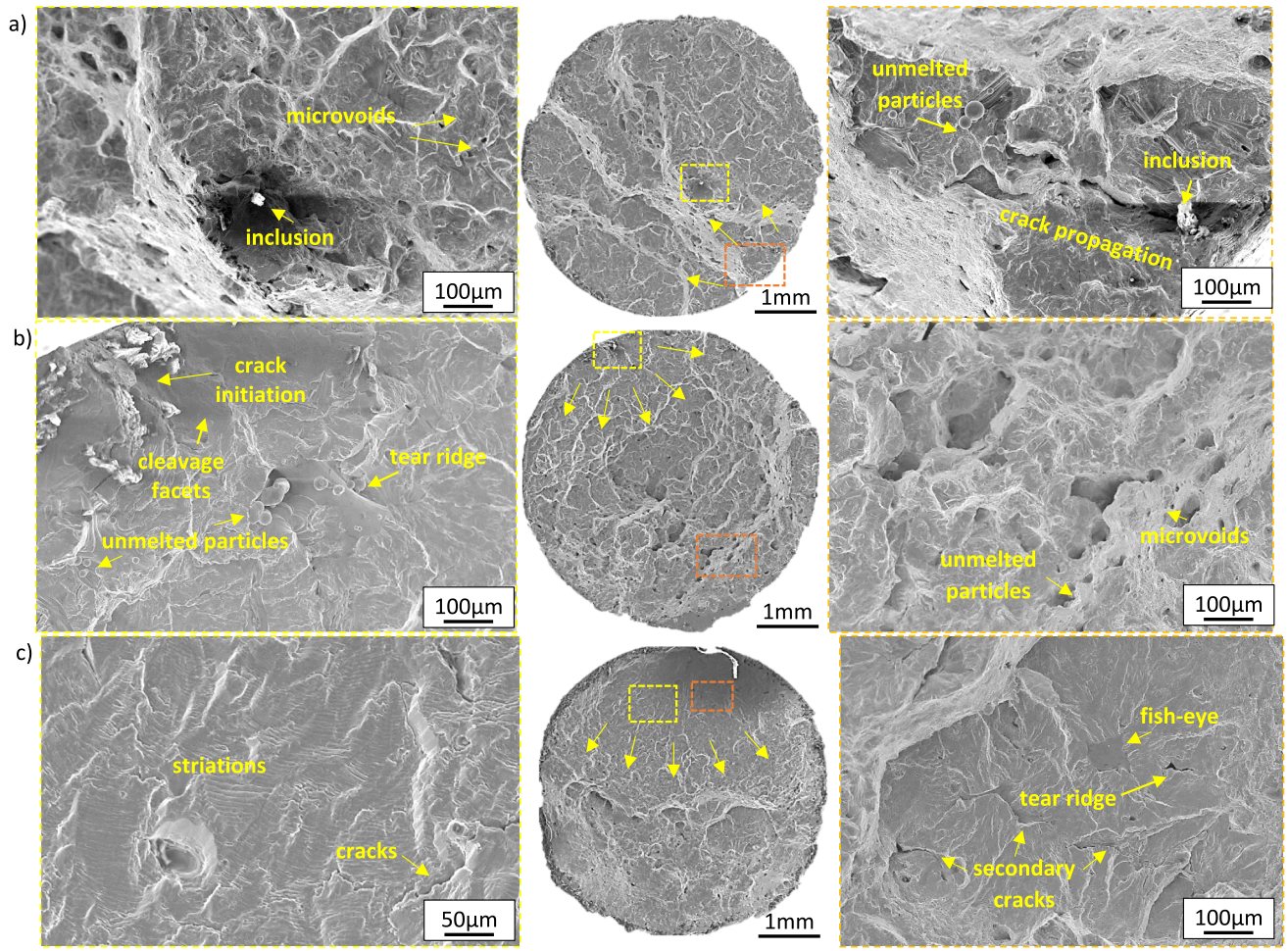


**Fig. 9** Fracture surfaces of SS316L specimens manufactured at Z (**a**), ZX (**b**), and XY (**c**) directions and tested at the stress amplitude equal to ±300 MPa

similar mode, near the specimen surface, the crack propagates steadily exhibiting a notable facets and cleavage facet formations (Fig. 9(b)). And the classical fracture zones including crack initiation, propagation, and instantaneous areas were distinguished in the XY-oriented specimen (Fig. 9(c)). For all samples subjected to fatigue testing at ±500 MPa, which is relatively close to the yield point of the material tested, a significantly larger area of ductile deformation was found (Fig. 8). Nonetheless some characteristic features (including unmelted or hard particles) acting as stress concentrators in all directions must be considered. The fracture surface analysis revealed secondary cracks that were associated with the delamination, due to the high-stress amplitude applied.

## Damage Parameters and Analysis of the Fatigue Damage Development

The S-N curve is the conventional approach that is effectively used to assess the effect of printing direction on the material integrity [39]. However, the comparison of the service life registered for the three printing orientations of the SS316L provides only a limited knowledge on fatigue damage development, FDD. Additionally, a determination of the typical S-N curve is time-consuming and expensive. The alternative method has been elaborated in [40] and further developed in [37, 41, 42]. It is based on the evolution of deformation dynamics development due to the ratcheting and cyclic plasticity registered in subsequent cycles as shown in Fig. 10. These changes were parametrized and described as the fatigue damage measure, ϕ, and the fatigue damage parameter D.

Since both mechanisms, ratcheting and cyclic plasticity, were observed for the SS316L, the combination of these damage indicators was defined as (equation (1)):

$$\varphi = \epsilon_w + \epsilon_m \tag{1}$$

where:

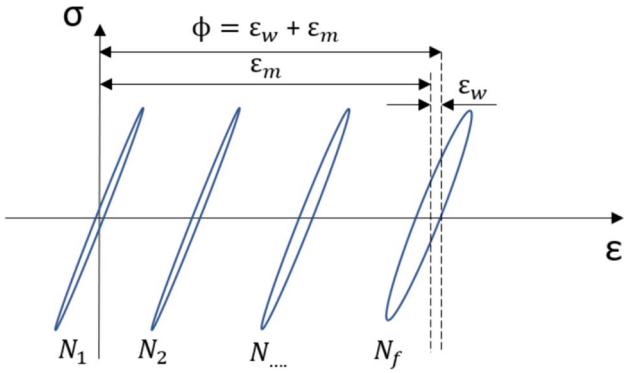


**Fig. 10** Evolution of the hysteresis loop in subsequent loading cycles

$\epsilon_w$ is the inelastic strain amplitude being the damage indicator that characterizes a width of the hysteresis loop at the total unloading,

$\epsilon_m$ is the mean inelastic strain responsible for a shift of the hysteresis loop under the unloaded state.

The inelastic strain amplitude captured at the total unloading of the material was described as (equation (2)):

$$\epsilon_w = \frac{\epsilon_{max}^{F=0} - \epsilon_{min}^{F=0}}{2} \tag{2}$$

The mean inelastic strain measured under the unloaded state was defined by the following relationship (equation (3)):

$$\epsilon_m = \frac{\epsilon_{min}^{F=0} + \epsilon_{max}^{F=0}}{2} \tag{3}$$

Changes in the fatigue damage measure, φ, were then used to determine evolution of the damage parameter D, which describes the dynamics of deformation changes in subsequent cycles (equation (4)):

$$D = \frac{\varphi_N - \varphi_{min}}{\varphi_{max} - \varphi_{min}} \tag{4}$$

where:

$\varphi_N$ is the current value of the FDD measure in the cycle $N$,

$\varphi_{min}$ is the minimum value of the FDD measure at the beginning of the cyclic loading, i.e. for the cycle $N=1$,

$\varphi_{max}$ is the maximum value of the FDD measure for the last cycle of the period of stable damage development $N_f$.

An evolution of the fatigue damage parameter in relation to the number of cycles to failure identifies the FDD dynamics. Figure 11 shows the development of fatigue damage for all samples tested at both low and high stress amplitudes. It was observed that XY, ZX and Z samples displayed significantly different characteristics of the process deterioration. The lines depict the typical evolution of parameter D for a single specific fatigue test and the shaded areas surrounding

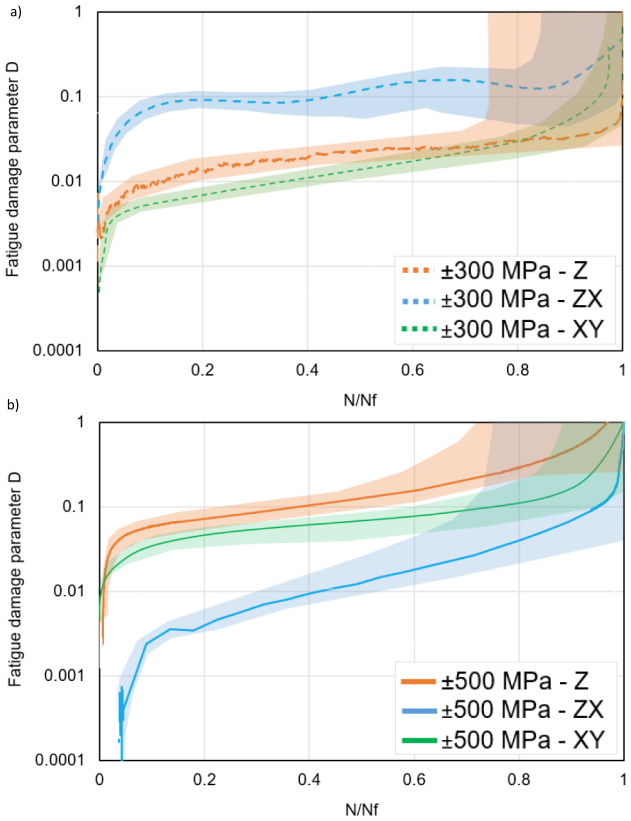


**Fig. 11** Development of the fatigue damage of SS316L for stress amplitude of ±300 MPa (**a**) and ±500 MPa (**b**), respectively, expressed by the fatigue damage parameter D evolution as a function of the number of cycles and current cycle/number of cycles to failure ratio

these lines represent the variation from 3 repeats. The $N_f$ number corresponds to the total number of cycles to failure for specific specimen, while N is the cycle number from the range 0 to $N_f$. Such representation enables the estimation of the length of the steady-state stage of fatigue, which represents the safe region of stable fatigue damage development. Based on the curves' character, three stages of FDD were recognised as follows:

Stage I: The elasto-plastic stage during which the parameter D increases to achieve a value corresponding to the stable level of strain accumulation; At this stage, fatigue damage starts at microstructural defects such as pores, grain boundaries and irregularities.

Stage II: The stable stage of strain accumulation characterized by the constant rate of FDD and described by a relatively low change of the parameter D; Micro-cracks are formed at in strain localised regions and starts to grow.

Stage III: A very quick strain accumulation leading to the dominant crack initiation, its rapid propagation, and finally, material decohesion that corresponds to the rapid increase of the parameter D. The multiple microcracks grow further

and start coalescing leading to larger cracks. When a critical crack size is reached, fracture happens.

The ideal scenario should include relatively short Stage I, long-term Stage II of slow and stable increase of D, and extended Stage III in comparison to typically observed, finished by specimen failure. A rapid increase of D in each stage may correspond to the specimen overloading or its plastic deformation (stage I), too early dominant crack formation (stage II) and accelerated dominant crack propagation (stage III).

An analysis of the fatigue damage parameter evolution shows that at both stress amplitudes ± 300 MPa and ± 500 MPa, the ZX samples exhibited notable growth in the initial cycles. However, its behaviour is different when the lower stress amplitude was applied (300 MPa). Once the D parameter reached the stable level of 0.1, the stable FDD was observed almost till the fracture. Conversely, when the higher stress amplitude of 500 MPa was applied an accelerated dynamics of FDD was observed. It suggests the earlier crack initiation and subsequent faster propagation in the remaining cycles. The Z and XY samples represented a stable, however notable, increase of fatigue damage parameter during the test. In such cases, the cracks initiated and propagated steadily till the dominant crack formation. Subsequently, there was a quickly approaching failure represented by the considerable, exponential increase of the fatigue damage parameter.

It can be observed in Fig. 11 that all AM specimens exhibited the three-staged behaviour. However, in the case of higher value of D parameter obtained at the beginning of fatigue test, a more stable steady-state stage was obtained. Such behaviour led to the undesirable increase of D parameter in the third stage, which corresponded to the rapid specimen failure. This phenomenon was clearly visible for the Z samples, which might be attributed to the weak metallurgical bond between layers of AM specimen.

Although the proposed damage parameter approach does not consider initial porosities, it provides more information than S-N curves or evolution of hysteresis loops in subsequent cycles as it clearly shown the damage dynamics from the beginning to the end of fatigue test. It is, however, very important to include as many material features as possible to clearly define the effect of initial microstructure on damage development due to fatigue.

## Conclusions

The suitability of the LPBF-M method to manufacture the SS316L specimens in three different directions of Z, ZX and XY was investigated through fatigue tests under force control using symmetric tension-compression cyclic loading and stress asymmetry coefficient equal to -1 in the range of stress amplitude from ± 300 MPa to ± 500 MPa. The following conclusions were drawn:

- The comparative measurements of Hall flow, apparent and tapped density confirmed that SS316L powder, reused for 25 times, is viable for the LPBF-M process. Using both the Carrs index and Hausner ratio as a comparative measure of the flowability of the powder feedstock, the results concluded there was no difference between the fresh and reused powder feedstock that was managed by sieving the oxides and abnormal powder particles in the powder bed using a 63 μm sieve.
- Printing in horizontal (XY) and diagonal (ZX) directions, with reused powder, improved the service life of the SS316L alloy in comparison to the vertical (Z). The same finding was observed for the fresh powder is used in the literature.
- The fracture surface analysis of Z, ZX, and XY-oriented samples subjected to varying stress amplitudes reveals distinct fracture mechanisms. In the Z samples, crack nucleation occurs near the surface, with unmelted particles, cleavage facets, and tear ridges evident, while the ZX samples show steady crack propagation with notable facet formations. The XY samples exhibit classical fracture zones with clear crack initiation, propagation, and instantaneous areas. At higher stress amplitudes (± 500 MPa), closer to the material's yield point, a larger area of ductile deformation is observed across all samples, with secondary cracks and delamination also present, indicating the significant impact of stress concentrators like unmelted or hard particles.
- An enhanced methodology for analysing variations in fatigue damage parameter D across multiple tests conducted under fixed conditions as a function of the number of cycles, was developed; It concluded cyclic plasticity and ratcheting to be the main mechanism of damage.

**Acknowledgements** The authors would like to express their gratitude to Mr M. Wyszkowski and Mr. M. Tarsała for their kind help during the experimental part of this work.

**Author Contributions** Conceptualization M.K.; Data curation M.K. and W.M.; Formal analysis M.K., P.W. and Z.K.; Investigation M.K., P.W. and G.W.; Methodology M.K., P.W., W.M. and Z.K.; Project administration M.K., P.W.; Supervision M.K.; Validation M.K., U.G., Z.K.; Visualization M.K.; Roles/Writing - original draft M.K.; Writing - review & editing Z.K., U.G., PW.

**Data Availability** The data will be shared upon reasonable requests.

## Declarations

**Conflict of Interest** The authors declare they have no financial interests.

## References

1. Avanzini A (2023) Fatigue behavior of additively manufactured stainless steel 316L. Mater 16(1):65
2. Bedmar J, Riquelme A, Rodrigo P, Torres B, Rams J (2021) Comparison of different additive manufacturing methods for 316L stainless steel. Mater 14(21):6504
3. D'Andrea D (2023) Additive manufacturing of AISI 316L stainless steel: a review. Metals 13(8):1370
4. Narasimharaju SR et al (2022) A comprehensive review on laser powder bed fusion of steels: processing, microstructure, defects and control methods, mechanical properties, current challenges and future trends. J Manuf Process 75:375–414. https://doi.org/10.1016/j.jmapro.2021.12.033
5. Li J, Liu W, Shen J, Zhang X, Li S, Wang Z (2024,) Research progress of the metal powder reuse for powder bed fusion additive manufacturing technology. Powder Technol 441:119815. https://doi.org/10.1016/j.powtec.2024.119815
6. Warner JH, Ringer SP, Proust G (2024) Strategies for metallic powder reuse in powder bed fusion: a review. J Manuf Process 110:263–290. https://doi.org/10.1016/j.jmapro.2023.12.066
7. Delacroix T, Lomello F, Schuster F, Maskrot H, Garandet J-P (2022) Influence of powder recycling on 316L stainless steel feedstocks and printed parts in laser powder bed fusion. Additive Manuf 50:102553. https://doi.org/10.1016/j.addma.2021.102553
8. Heiden MJ et al (2019) Evolution of 316L stainless steel feedstock due to laser powder bed fusion process. Additive Manuf 25:84–103. https://doi.org/10.1016/j.addma.2018.10.019
9. Gorji NE, O'Connor R, Mussatto A, Snelgrove M, González PGM, Brabazon D (2019) Recyclability of stainless steel (316 L) powder within the additive manufacturing process. Materialia 8:100489. https://doi.org/10.1016/j.mtla.2019.100489
10. Abdelwahed M, Casati R, Larsson A, Petrella S, Bengtsson S, Vedani M (2022) On the recycling of water atomized powder and the effects on properties of L-PBF processed 4130 low-alloy steel. Mater 15(1)
11. Schur R et al (2020) A fractographic analysis of additively manufactured Ti6Al4V by electron beam melting: effects of powder reuse. J Fail Anal Prev 20, 3:794–803. https://doi.org/10.1007/s11668-020-00875-0
12. Smith TR, Sugar JD, San Marchi C, Schoenung JM (2017) Orientation Effects on Fatigue Behavior of Additively Manufactured Stainless Steel. In: ASME 2017 Pressure Vessels and Piping Conference, vol. 6A: Materials and Fabrication, V06AT06A020. [Online]. Available: https://doi.org/10.1115/PVP2017-65948
13. Yang N et al (2017) Process-structure-property relationships for 316L stainless steel fabricated by additive manufacturing and its implication for component engineering. J Therm Spray Technol 26(4):610–626. https://doi.org/10.1007/s11666-016-0480-y
14. Guo P, Zou B, Huang C, Gao H (2017) Study on microstructure, mechanical properties and machinability of efficiently additive manufactured AISI 316L stainless steel by high-power direct laser deposition. J Mater Process Technol 240:12–22. https://doi.org/10.1016/j.jmatprotec.2016.09.005
15. Mower TM, Long MJ (2016) Mechanical behavior of additive manufactured, powder-bed laser-fused materials. Mater Sci Engineering: A 651:198–213. https://doi.org/10.1016/j.msea.2015.10.068
16. Blinn B, Ley M, Buschhorn N, Teutsch R, Beck T (2019) Investigation of the anisotropic fatigue behavior of additively manufactured structures made of AISI 316L with short-time procedures PhyBaLLIT and PhyBaLCHT. Int J Fatigue 124:389–399. https://doi.org/10.1016/j.ijfatigue.2019.03.022
17. Fergani O, Bratli Wold A, Berto F, Brotan V, Bambach M (2018) Study of the effect of heat treatment on fatigue crack growth behaviour of 316L stainless steel produced by selective laser melting. Fatigue Fract Eng Mater Struct 41(5):1102–1119. https://doi.org/10.1111/ffe.12755
18. Douglas R, Barnard N, Lavery N, Sullivan J, Jones T, Lancaster R (2024) The effect of powder recycling on the mechanical performance of laser powder bed fused stainless steel 316L. Additive Manuf 88:104245. https://doi.org/10.1016/j.addma.2024.104245
19. Renishaw (2017) SS 316L-0407 powder for additive manufacturing, Online, [Online]. Available: https://www.renishaw.com/resourcecentre/en/details/Data-sheet-SS-316L-0407-powder-for-additive-manufacturing--90802?lang=en&srsltid=AfmBOoo7rSiciblx_AcftrWgHyivhWOyZ7QO2pHTYpkmz1fC2S2mSepT. Accessed 10 July 2024
20. Yusuf SM, Chen Y, Boardman R, Yang S, Gao N (2017) Investigation on porosity and microhardness of 316L stainless steel fabricated by selective laser melting. Metals 7(2):64
21. Powell D, Rennie AEW, Geekie L, Burns N (2020) Understanding powder degradation in metal additive manufacturing to allow the upcycling of recycled powders. J Clean Prod 268:122077. https://doi.org/10.1016/j.jclepro.2020.122077
22. Alsalla HH, Smith C, Hao L (2018) Effect of build orientation on the surface quality, microstructure and mechanical properties of selective laser melting 316L stainless steel. Rapid Prototyp J 24(1):9–17. https://doi.org/10.1108/RPJ-04-2016-0068
23. Wood P, Libura T, Kowalewski ZL, Williams G, Serjouei A (2019) Influences of horizontal and vertical build orientations and post-fabrication processes on the fatigue behavior of stainless steel 316L produced by selective laser melting. Mater (Basel) 12(24):4203. https://doi.org/10.3390/ma12244203
24. Kunz J, Kaletsch A, Broeckmann C (2017) Influence of the building position and post HIP treatment on properties of SLM components. In: The conference proceedings by the European Powder Metallurgy Association (EPMA), As presented at Euro PM2017 Congress and Exhibition, Milan, Italy, 1–5 October 2017
25. Mussatto A et al (2022) Assessing dependency of part properties on the printing location in laser-powder bed fusion metal additive manufacturing. Mater Today Commun 30:103209. https://doi.org/10.1016/j.mtcomm.2022.103209
26. Li Z, Xu R, Zhang Z, Kucukkoc I (2018) The influence of scan length on fabricating thin-walled components in selective laser melting. Int J Mach Tools Manuf 126:1–12. https://doi.org/10.1016/j.ijmachtools.2017.11.012
27. Hao L, Wang W, Zeng J, Song M, Chang S, Zhu C (2023) Effect of scanning speed and laser power on formability, microstructure, and quality of 316L stainless steel prepared by selective laser melting. J Mater Res Technol 25:3189–3199. https://doi.org/10.1016/j.jmrt.2023.06.144
28. Zhang M et al (2019) High cycle fatigue life prediction of laser additive manufactured stainless steel: a machine learning approach. Int J Fatigue 128:105194. https://doi.org/10.1016/j.ijfatigue.2019.105194

29. Blinn B, Krebs F, Ley M, Teutsch R, Beck T (2020) Determination of the influence of a stress-relief heat treatment and additively manufactured surface on the fatigue behavior of selectively laser melted AISI 316L by using efficient short-time procedures. Int J Fatigue 131:105301. https://doi.org/10.1016/j.ijfatigue.2019.105301
30. Riemer A, Leuders S, Thöne M, Richard HA, Tröster T, Niendorf T (2014) On the fatigue crack growth behavior in 316L stainless steel manufactured by selective laser melting. Eng Fract Mech 120:15–25. https://doi.org/10.1016/j.engfracmech.2014.03.008
31. Afkhami S, Dabiri M, Piili H, Björk T (2021) Effects of manufacturing parameters and mechanical post-processing on stainless steel 316L processed by laser powder bed fusion. Mater Sci Eng: A 802:140660. https://doi.org/10.1016/j.msea.2020.140660
32. Lai W-J, Ojha A, Li Z, Engler-Pinto C, Su X (2021) Effect of residual stress on fatigue strength of 316L stainless steel produced by laser powder bed fusion process. Progress Additive Manuf 6(3):375–383. https://doi.org/10.1007/s40964-021-00164-8
33. Duan H et al (2023) Prediction of 316 stainless steel low-cycle fatigue life based on machine learning. Sci Rep 13(1):6753. https://doi.org/10.1038/s41598-023-33354-1
34. Zhan Z, Li H (2021) Machine learning based fatigue life prediction with effects of additive manufacturing process parameters for printed SS 316L. Int J Fatigue 142:105941. https://doi.org/10.1016/j.ijfatigue.2020.105941
35. Nafar Dastgerdi J, Jaberi O, Remes H, Lehto P, Hosseini Toudeshky H, Kuva J (2023) Fatigue damage process of additively manufactured 316 L steel using X-ray computed tomography imaging. Additive Manuf 70:103559. https://doi.org/10.1016/j.addma.2023.103559
36. Kopec M (2023) Fatigue damage development in 14MoV6-3 steel for power plant pipes monitored by digital image correlation. Acta Mech Solida Sin 36(3):405–417. https://doi.org/10.1007/s10338-023-00387-y
37. Kopec M, Kukla D, Brodecki A, Kowalewski ZL (2021) Effect of high temperature exposure on the fatigue damage development of X10CrMoVNb9-1 steel for power plant pipes. Int J Press Vessels Pip 189:104282. https://doi.org/10.1016/j.ijpvp.2020.104282
38. Macek W, Branco R, Podulka P, Kopec M, Zhu S-P, Domingos CJ (2023) A brief note on entire fracture surface topography parameters for 18Ni300 maraging steel produced by LB-PBF after LCF. Eng Fail Anal 153:107541. https://doi.org/10.1016/j.engfailanal.2023.107541
39. Silva JA, Caetano DA, Ribeiro Filho SLM, Teixeira FN, Guimarães LGM (2022) Calculation and enhancement of fatigue life by ε-N approach and corrosion fatigue in steam turbine rotor. Int J Damage Mech 31(6):845–863. https://doi.org/10.1177/10567895221082209
40. Socha G, Dietrich L (2014) A fatigue damage indicator parameter for P91 chromium-molybdenum alloy steel and fatigue predamaged P54T carbon steel. Fatigue Fract Eng Mater Struct 37(2):195–205. https://doi.org/10.1111/ffe.12104
41. Kukla D, Kowalewski Z, Grzywna P, Kubiak K (2014) Assessment of fatigue damage development in power engineering steel by local strain analysis. Kovove Mater 52(01):269–277. https://doi.org/10.4149/km_2014_5_269
42. Rutecka A, Kowalewski A, Makowska K, Pietrzak K, Dietrich L (2015) Fatigue damage of Al/SiC composites - macroscopic and microscopic analysis. Arch Metall Mater 60(1). https://doi.org/10.1515/amm-2015-0016